DIOXYGEN ACTIVATION

Reactive high-spin iron(IV)-oxo sites through dioxygen activation in a metal–organic framework

Kaipeng Hou[1,2]†, Jonas Börgel[1,2]†, Henry Z. H. Jiang[1], Daniel J. SantaLucia[3,4], Hyunchul Kwon[1], Hao Zhuang[5,6], Khetpakorn Chakarawet[7]‡, Rachel C. Rohde[1], Jordan W. Taylor[1], Chaochao Dun[8], Maria V. Paley[1,2]§, Ari B. Turkiewicz[1], Jesse G. Park[1]¶, Haiyan Mao[5], Ziting Zhu[2,6], E. Ercan Alp[9], Jiyong Zhao[9], Michael Y. Hu[9], Barbara Lavina[9,10], Sergey Peredkov[3], Xudong Lv[1], Julia Oktawiec[11], Katie R. Meihaus[1], Dimitrios A. Pantazis[4], Marco Vandone[12], Valentina Colombo[12,13], Eckhard Bill[3], Jeffrey J. Urban[2,8], R. David Britt[7,14], Fernande Grandjean[15], Gary J. Long[15], Serena DeBeer[3], Frank Neese[4], Jeffrey A. Reimer[2,5], Jeffrey R. Long[1,2,5]*

In nature, nonheme iron enzymes use dioxygen to generate high-spin iron(IV)=O species for a variety of oxygenation reactions. Although synthetic chemists have long sought to mimic this reactivity, the enzyme-like activation of O_2 to form high-spin iron(IV)=O species remains an unrealized goal. Here, we report a metal–organic framework featuring iron(II) sites with a local structure similar to that in α-ketoglutarate-dependent dioxygenases. The framework reacts with O_2 at low temperatures to form high-spin iron(IV)=O species that are characterized using in situ diffuse reflectance infrared Fourier transform, in situ and variable-field Mössbauer, Fe Kβ x-ray emission, and nuclear resonance vibrational spectroscopies. In the presence of O_2, the framework is competent for catalytic oxygenation of cyclohexane and the stoichiometric conversion of ethane to ethanol.

The development of catalysts for the selective oxygenation of light hydrocarbons using O_2 remains a formidable but important challenge in the global effort to develop green technologies for the valorization of natural gas components (*1*–*3*). Nature has developed mononuclear nonheme iron metalloenzymes that use O_2 for C–H oxygenation chemistry, such as the ubiquitous α-ketoglutarate-dependent dioxygenases (*4*). One well-studied enzyme in this class is taurine–α-ketoglutarate dioxygenase (TauD), which oxygenates one of the C–H bonds of taurine alpha to the sulfonate group (*5*). Key to the reactivity of TauD and its family of dioxygenases is a high-spin (S = 2) Fe(IV)=O intermediate, which is formed following oxidation of iron(II) with O_2 coupled with oxidation and decarboxylation of the α-ketoglutarate co-substrate (Fig. 1A) (*6*, *7*). Over the last several decades, significant research effort has been devoted to the design and study of iron(IV)–oxo species in molecular (*8*–*17*) and iron–zeolite (*18*, *19*) model systems in order to better understand and mimic their reactivity in biological systems. However, most examples studied to date feature an intermediate spin ground state (S = 1), and only a small number of these are generated using dioxygen in solution (*10*–*13*). High-spin Fe(IV)=O species have been accessed with oxidants such as trimethylammonium-*N*-oxide, hypervalent iodine reagents, and nitrous oxide (*14*, *15*, *18*), as well as in the presence of O_2 with light irradiation to cleave the O–O bond (*17*). However, the use of O_2 alone for the generation of high-spin Fe(IV)=O species, in a manner akin to metalloenzyme reactivity, has yet to be achieved in any synthetic system (*16*, *19*, *20*).

Metal–organic frameworks have received increasing attention in recent years as attractive systems for studying biomimetic chemistry (*21*–*23*). These porous, crystalline solids are constructed from metal nodes and organic linkers and exhibit chemical and structural tunability unmatched in other porous materials (*24*, *25*). As such, metal–organic frameworks offer the opportunity to explore O_2 activation in solid–gas reactions, while the immobilization of metal sites in the lattice may serve to prevent the decomposition of reactive species through dimerization or intramolecular ligand oxidation pathways available to molecular compounds (*9*, *26*, *27*). However, reported mimics of nonheme iron enzymes in metal–organic frameworks are scarce (*28*). In this context, framework $Fe_{1.5}Zn_{3.5}Cl_4(btdd)_3$ (H_2btdd = (1*H*-1,2,3-triazolo [4,5-*b*],[4′,5′-*i*])dibenzo[1,4]dioxin) (*29*) stands out as a suitable biomimetic platform (*22*). This material is synthesized through postsynthetic iron(II) exchange in $Zn_5Cl_4(btdd)_3$ (MFU-4*l*) (*30*) and features pseudo-tetrahedral iron(II) sites with tris(triazolate) coordination reminiscent of the binding of the 2-His-1-carboxylate facial triad in TauD. Herein, we report the frameworks $Fe_xZn_{5-x}(prv)_4(btdd)_3$ (x = 1 or 1.8; Hprv = pyruvic acid) and $FeZn_4(moba)_4(btdd)_3$ (Hmoba = 3,3-dimethyl-2-oxobutanoic acid), which react with O_2 to generate high-spin (S = 2) Fe(IV)=O species that are reactive toward hydrocarbon oxygenation (Fig. 1, B and C).

Synthesis and characterization of $Fe_xZn_{5-x}(prv)_4(btdd)_3$

The frameworks $Fe_xZn_{5-x}(prv)_4(btdd)_3$ were prepared through post-synthetic cation exchange in $Zn_5Cl_4(btdd)_3$ using ferrous chloride and subsequent ligand exchange with pyruvate (see supplementary materials). Energy-dispersive x-ray (EDX) spectroscopy revealed that the iron sites in $Fe_xZn_{5-x}Cl_4(btdd)_3$ are homogeneously distributed within the materials (figs. S1 and S2), and inductively coupled plasma optical emission spectroscopy (ICP-OES) confirmed the extent of iron substitution. Quantitative exchange of chloride for pyruvate in $Fe_xZn_{5-x}(prv)_4(btdd)_3$ is supported by elemental analysis (see section 1.3 of the SM).

Powder x-ray diffraction analysis confirmed that the $Fe_xZn_{5-x}(prv)_4(btdd)_3$ materials are crystalline solids and isostructural to the parent MFU-4*l* framework (fig. S3), and N_2 adsorption data obtained at 77 K revealed high Brunauer–Emmett–Teller (BET) surface areas of 2130 ± 12 and 2090 ± 15 m^2/g for x = 1 and 1.8, respectively (figs. S4 and S5). The 5 K Mössbauer spectrum of desolvated $FeZn_4(prv)_4(btdd)_3$ features a major doublet [area of 84.2(8)%] with an isomer shift (δ) of 1.061(1) mm/s and a quadrupole splitting ($|\Delta E_Q|$) of 2.567(1) mm/s, indicative of high-spin, five-coordinate iron(II) (fig. S18) (*31*). Two minor doublets with slightly different Mössbauer parameters likely correspond to six-coordinate iron(II) sites featuring residual coordinating synthesis solvent (table S5). The magnetic circular dichroism spectrum of

[1]Department of Chemistry, University of California, Berkeley, CA 94720, USA. [2]Materials Sciences Division, Lawrence Berkeley National Laboratory, Berkeley, CA 94720, USA. [3]Max Planck Institute for Chemical Energy Conversion, D-45470 Mülheim an der Ruhr, Germany. [4]Max-Planck-Institut für Kohlenforschung, D-45470 Mülheim an der Ruhr, Germany. [5]Department of Chemical and Biomolecular Engineering, University of California, Berkeley, CA 94720, USA. [6]Department of Materials Science and Engineering, University of California, Berkeley, CA 94720, USA. [7]Department of Chemistry, University of California, Davis, CA 95616, USA. [8]The Molecular Foundry, Lawrence Berkeley National Laboratory, Berkeley, CA 94720, USA. [9]Advanced Photon Source, Argonne National Laboratory, Lemont, IL 60439, USA. [10]Center for Advanced Radiation Sources, The University of Chicago, Chicago, IL 60637, USA. [11]Department of Chemistry, Northwestern University, Evanston, IL 60208, USA. [12]Department of Chemistry, University of Milan, 20133 Milan, Italy. [13]Consorzio Interuniversitario Nazionale per la Scienza e Tecnologia dei Materiali (INSTM), UdR Milano, Via Golgi 19, 20133 Milano, Italy. [14]Miller Institute for Basic Research in Science, University of California, Berkeley CA 94720, USA [15]Department of Chemistry, Missouri University of Science and Technology, University of Missouri, Rolla, MO 65409, USA.
*Corresponding author. Email: jrlong@berkeley.edu
†These authors contributed equally to this work.
‡Present address: Department of Chemistry, Faculty of Science, Mahidol University, Bangkok 10400, Thailand.
§Present address: ChemFinity Technologies, Inc., 710 Parkside Ave, Brooklyn, NY 11226.
¶Present address: Department of Chemistry, Korea Advanced Institute of Science and Technology (KAIST), Daejeon 34141, Republic of Korea.

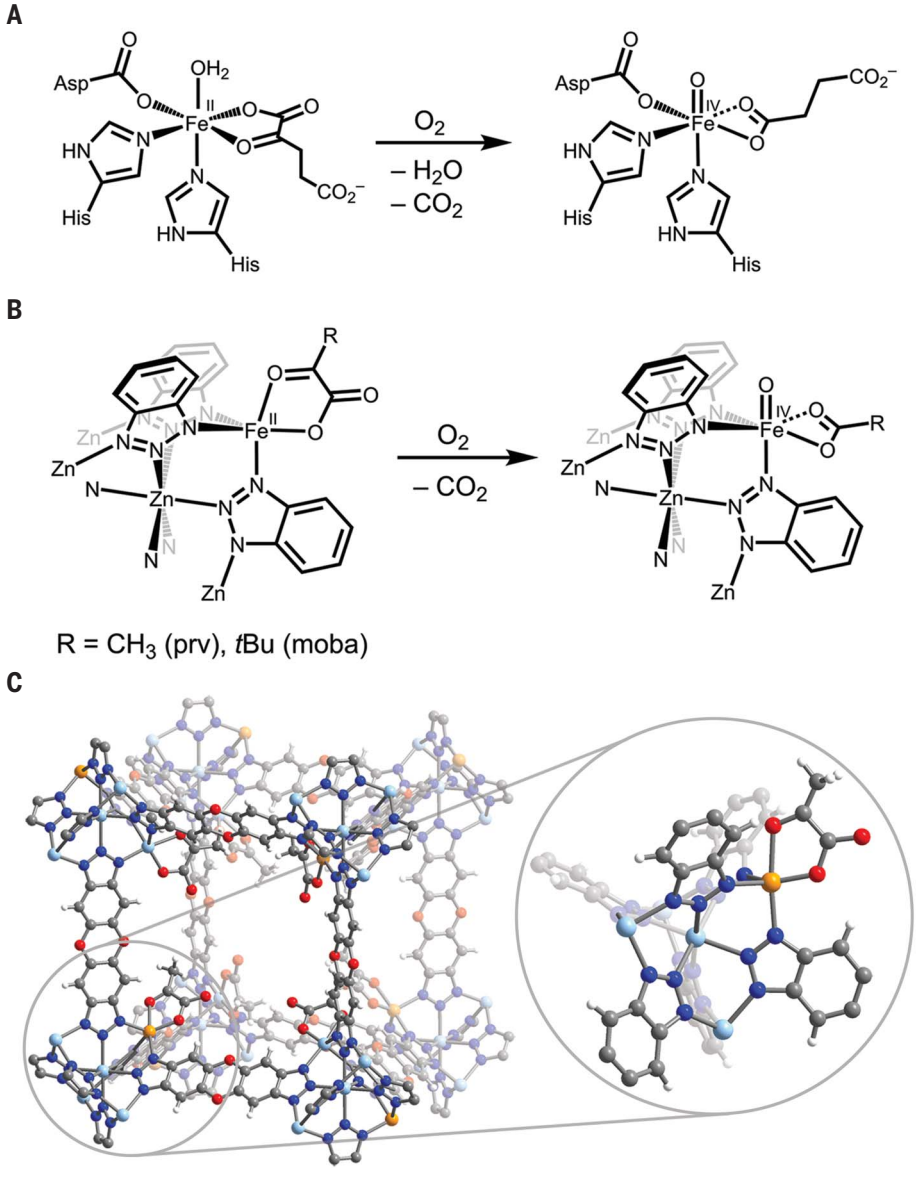

Fig. 1. Design of a metal–organic framework mimic of taurine–α-ketoglutarate dioxygenase (TauD). (**A**) Illustration of the local structure of the mononuclear nonheme iron(II) sites in TauD and generation of the reactive high-spin Fe(IV)=O species (TauD-*J*) through oxidation with O_2 coupled with decarboxylation of the α-ketoglutarate co-substrate. (**B**) Illustration of the local coordination environment of the iron(II) sites in $FeZn_4(prv)_4(btdd)_3$ (R = CH_3) or $FeZn_4(moba)_4(btdd)_3$ (R = *t*Bu) and observed reactivity with O_2 at low temperatures to form an Fe(IV)=O species coordinated by acetate or pivalate formed through the decarboxylation of pyruvate (prv) or 3,3-dimethyl-2-oxobutyrate (moba), respectively. (**C**) (Left) Illustration of a cubic pore within $FeZn_4(prv)_4(btdd)_3$ derived using single-crystal x-ray diffraction data obtained for $Zn_5(prv)_4(btdd)_3$ (fig. S15B) and (right) expanded view of the truncated structure of a cluster node of the framework showing the nature of the pyruvate coordination, as supported by Mössbauer, magnetic circular dichroism, and nuclear resonance vibrational spectroscopies. Light blue, orange, red, blue, gray, and white spheres represent Zn, Fe, O, N, C, and H atoms, respectively.

$FeZn_4(prv)_4(btdd)_3$ collected at 5 K under a field of 7 T features d-d transitions around 6000 and 14,000 cm^{-1}, which are consistent with $S = 2$ iron(II) centers in a five-coordinate ligand field (fig. S8). Continuous-wave parallel mode electron paramagnetic resonance (EPR) spectroscopy and dc magnetic susceptibility data collected for $Fe_xZn_{5-x}(prv)_4(btdd)_3$ further support the assignment of $S = 2$ for the iron(II) sites (figs. S9 to S11).

We turned to solid-state ^{1}H NMR spectroscopy to gain more insight into the possible binding modes of the pyruvate ligands in $FeZn_4(prv)_4(btdd)_3$. The spectrum exhibits broad features owing to the paramagnetic sites, which preclude the extraction of meaningful information (fig. S12). As such, we prepared a crystalline powder sample of $Zn_5(prv)_4(btdd)_3$ featuring pyruvate labeled with ^{13}C at the methyl carbon. The solid-state ^{1}H NMR spectrum features resonances from the protons of the $btdd^{2-}$ linker and the pyruvate methyl group in a ~1:1 ratio, supporting quantitative ligand exchange (fig. S13). We were also able to prepare single crystals of $Zn_5(prv)_4(btdd)_3$ (see sections 1.6 and 1.7 of the SM), and analysis through single-crystal x-ray diffraction revealed that pyruvate coordinates to the peripheral zinc(II) centers in a bidentate fashion (figs. S14B and S15B). It was not possible to isolate single crystals of $FeZn_4(prv)_4(btdd)_3$ through single-crystal-to-single-crystal exchange starting from $Zn_5Cl_4(btdd)_3$. However, the powder x-ray diffraction patterns of $Fe_xZn_{5-x}(prv)_4(btdd)_3$ are consistent with the simulated pattern generated for $Zn_5(prv)_4(btdd)_3$ from the single-crystal structure (fig. S3), which may indicate that the coordination mode of the pyruvate ligand is similar in the three frameworks.

In situ DRIFTS analysis of the reactivity of $Fe_{1.8}Zn_{3.2}(prv)_4(btdd)_3$ with O_2

Reactivity between $Fe_xZn_{5-x}(prv)_4(btdd)_3$ and O_2 was examined with variable temperature in situ diffuse reflectance infrared Fourier transform spectroscopy (DRIFTS) (fig. S16). For this purpose, we used $Fe_{1.8}Zn_{3.2}(prv)_4(btdd)_3$ with the goal of maximizing the resulting spectral signal whereas $FeZn_4(prv)_4(btdd)_3$ was used for the remaining spectroscopic analyses described below. Following dosing of a sample of desolvated $Fe_{1.8}Zn_{3.2}(prv)_4(btdd)_3$ with O_2 at 100 K, a new absorption band gradually appeared in the DRIFTS spectrum at 2341 cm^{-1}, which we assign as the asymmetric C=O stretch of physisorbed CO_2 formed from decarboxylation of pyruvate (Fig. 2A, solid lines). The intensity of this band increased as the temperature was increased to 150 and 200 K; above 250 K the band disappeared, consistent with CO_2 desorption from the framework. To verify that the detected CO_2 was derived from pyruvate and not from O_2, we carried out an analogous in situ experiment using $Fe_{1.8}Zn_{3.2}(1\text{-}^{13}C\text{-}prv)_4(btdd)_3$ (1-^{13}C-prv$^-$ = pyruvate labeled with ^{13}C on the carboxylate carbon atom) and $^{18}O_2$ (Fig. 2A, dashed lines). Upon dosing with $^{18}O_2$ at 100 K, a new stretch appeared at 2275 cm^{-1}, consistent with formation of the isotopologue $^{13}CO_2$ and not $^{13}C^{18}O_2$, confirming that the oxygen atoms do not originate from dioxygen. The $^{13}CO_2$ stretch grew in intensity with heating to 200 K and disappeared at higher temperatures. A slight deviation of the experimental CO_2 stretching frequencies reported herein from the values associated with gas-phase CO_2 (2349 and 2284 cm^{-1} for CO_2 and $^{13}CO_2$, respectively)

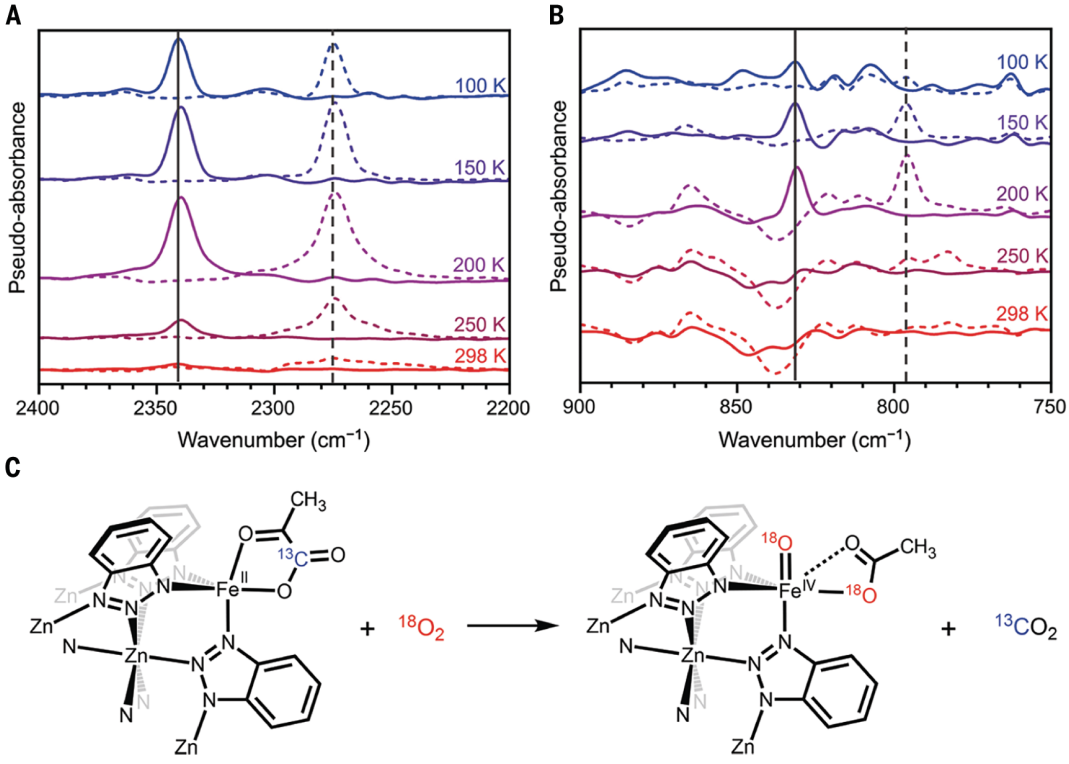

Fig. 2. Investigation of reactivity between $Fe_{1.8}Zn_{3.2}(prv)_4(btdd)_3$ and O_2 using variable-temperature in situ DRIFTS. (**A**) Spectra obtained after dosing $Fe_{1.8}Zn_{3.2}(prv)_4(btdd)_3$ with 20 mbar of O_2 at 100 K and gradually warming to 298 K (solid lines). The peak at 2341 cm^{-1} corresponds to CO_2 formed from the decarboxylation of pyruvate. This peak shifts to ~2275 cm^{-1} when $Fe_{1.8}Zn_{3.2}(1\text{-}^{13}C\text{-}prv)_4(btdd)_3$ is dosed with $^{18}O_2$ under the same conditions (dashed lines), consistent with formation of the isotopologue $^{13}CO_2$. (**B**) Spectra obtained as described in (A) showing the signature peaks for the iron(IV)=O species formed from the reaction between $Fe_{1.8}Zn_{3.2}(prv)_4(btdd)_3$ and O_2 (831 cm^{-1}) and $Fe_{1.8}Zn_{3.2}(1\text{-}^{13}C\text{-}prv)_4(btdd)_3$ and $^{18}O_2$ (796 cm^{-1}). All data shown correspond to difference spectra obtained using the desolvated iron(II) frameworks as the background. Minor differences in the intensities of the absorption bands for the natural abundance and heavier isotopologue samples are likely due to differences in powder sample mass, sample distribution in the background matrix, and slight positioning differences in the infrared beam. (**C**) The reaction probed by DRIFTS, wherein for simplicity, $FeZn_4(1\text{-}^{13}C\text{-}prv)_4(btdd)_3$ is shown to react with $^{18}O_2$.

can be ascribed to adsorption of the CO_2 within the pores of the framework at low temperatures. Notably, in situ powder x-ray diffraction data collected for $FeZn_4(prv)_4(btdd)_3$ after dosing with O_2 at 100 K over the course of gradual warming to 298 K revealed that the material remains highly crystalline under these conditions (fig. S24).

An absorption band was observed to grow in at 831 cm^{-1} upon dosing $Fe_{1.8}Zn_{3.2}(prv)_4(btdd)_3$ with O_2 at 100 K, which we assign as an Fe(IV)=O stretch (Fig. 2B, solid lines). This band increased in intensity with heating up to 200 K before diminishing significantly at 250 K and disappearing at 298 K. When the analogous experiment was performed with $^{18}O_2$, the band shifted to 796 cm^{-1}, consistent with a stretching frequency of 794 cm^{-1} calculated for Fe(IV) = ^{18}O using a simple harmonic oscillator model (Fig. 2B, dashed lines). For comparison, the Fe(IV) = ^{16}O and Fe(IV) = ^{18}O stretches in TauD-*J* appear at 821 and 787 cm^{-1}, respectively (*32*). Concomitant with the disappearance of the Fe(IV)=O stretch at 250 K, a new stretch appeared at 3628 cm^{-1} (fig. S17). We attribute this stretch to an Fe(III)–OH species arising from decomposition of the Fe(IV)=O through hydrogen-atom abstraction, possibly from the methyl group of the newly formed acetate ligand (Fig. 2C). At 298 K, a new stretch was apparent at 3678 cm^{-1} (fig. S17), which may correspond to a different coordination environment for the Fe(III)–OH species at higher temperatures. When $^{18}O_2$ was used for dosing, a stretch appeared at 3617 cm^{-1}, in excellent agreement with that calculated for Fe(III)–^{18}OH using a simple harmonic oscillator model (3616 cm^{-1}).

Experimental and computational investigation of the Fe(IV)=O spin state

The species formed upon reaction of $Fe_xZn_{5-x}(prv)_4(btdd)_3$ with dioxygen were further investigated by in situ Mössbauer spectroscopy (see section 2.9.1 of the SM). As discussed above, the 5 K Mössbauer spectrum of desolvated $FeZn_4(prv)_4(btdd)_3$ features a major doublet indicative of high-spin, five-coordinate iron (II) (Fig. 3A and table S6). After dosing with 300 mbar of O_2 at 100 K, this doublet persisted and a new doublet was apparent with δ = 0.260(4) mm/s and $|\Delta E_Q|$ = 0.572(8) mm/s [16.7(2)% area], which we assign to an Fe(IV)=O species. These parameters are similar to those determined for the S = 2 Fe(IV)=O intermediate of TauD (δ = 0.31 mm/s and ΔE_Q = −0.88 mm/s) (*6*, *7*). A detailed comparison with isomer shift and quadrupole splitting values for other reported iron(IV)–oxos reveals that they are more consistent with an S = 2 spin state ($\delta_{S=2}$ = 0.02–0.37 mm/s; $|\Delta E_Q|_{S=2}$ = 0.23–1.27 mm/s) than an S = 1 spin state ($\delta_{S=1}$ < 0.20 mm/s; $|\Delta E_Q|_{S=1}$ = 0.44–2.09 mm/s) (see fig. S40). Density functional theory (DFT) calculations at the B3LYP/def2-TZVP level of theory predict an isomer shift of 0.25 mm/s for an S = 2 six-coordinate Fe(IV)=O moiety featuring acetate coordinated in a κ^2-binding mode, in excellent agreement with the experimental value (tables S6 and S9).

We considered that a slow oxidation rate at 100 K may be a factor limiting the Fe(IV)=O content in O_2-dosed $FeZn_4(prv)_4(btdd)_3$. Indeed, the percent area of the Fe(IV)=O doublet could be increased up to a maximum of 20.0(2)% upon further dosing with of O_2 at 125 and 150 K. (Fig. 3A and table S6). However, subsequent dosing at 163 K did not result in an increase in the percent of the Fe(IV)=O doublet (figs. S19 and

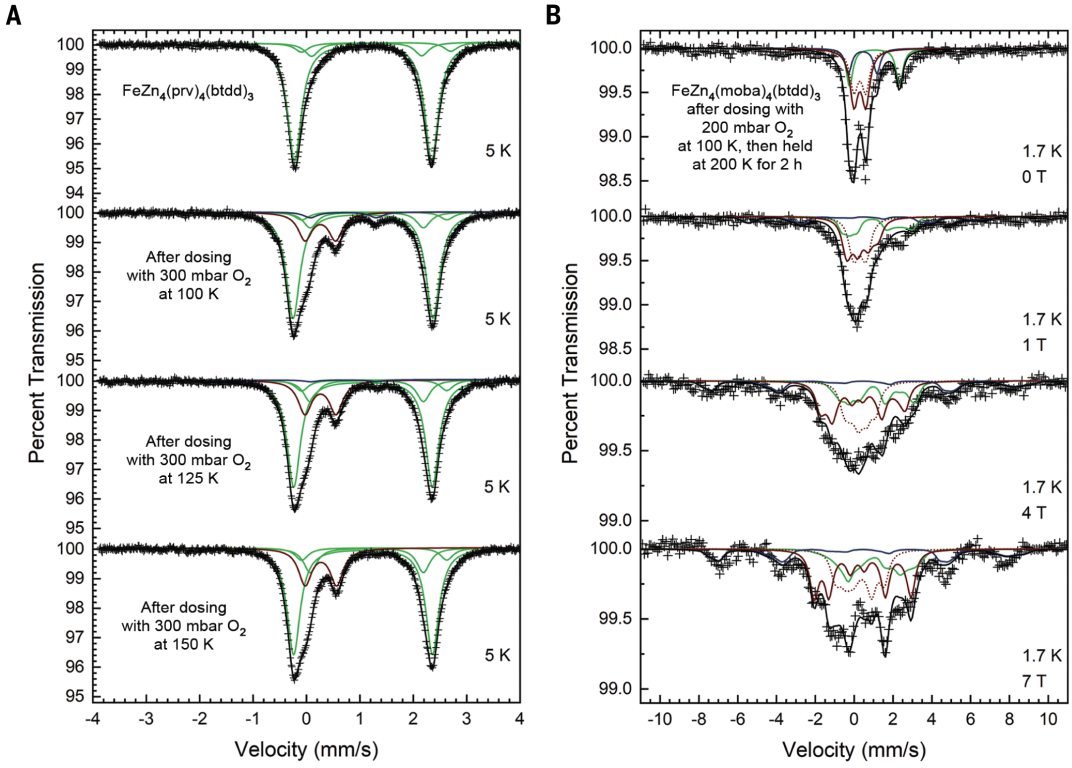

Fig. 3. In situ and variable-field Mössbauer spectra. (**A**) In situ Mössbauer spectra collected at 5 K for desolvated $FeZn_4(prv)_4(btdd)_3$ before and after dosing with 300 mbar of O_2 at 100, 125, and 150 K. All spectra were fit with a minimum number of symmetric quadrupole doublets, all of which have the same linewidth for a given spectrum (see fig. S22 for a timeline of the in situ dosing experiment). Green, blue, and dark red subspectra are consistent with iron(II), iron(III), and iron(IV) species, respectively (**B**) Variable magnetic field Mössbauer spectra collected at 1.7 K and the indicated fields for a sample of $FeZn_4(moba)_4(btdd)_3$ that had been dosed with 100 mbar of O_2 at 100 K, held for 2 hours at 200 K and subsequently dosed with 200 mbar of O_2 at 100 K and then warmed again at 200 K for 2 hours. Green, blue, dark red solid, and dark red dotted subspectra, respectively, were modeled as S = 2 iron(II), S = $^5/_2$ iron(III), isolated S = 2 Fe(IV)═O species, and S = 0 species arising from antiferromagnetic coupling between Fe(IV)═O species within the same node. The spectra were modeled as described in the main text to extract D = 12.7(6) cm^{-1} and A_{iso} = −16.4(4) T for the uncoupled Fe(IV)═O species (see table S13). Note, the width of the spectral splitting for the red trace at 7 T is smaller than has been observed for other S = 2 Fe(IV)═O species in the literature (~5 versus ~8 mm/s, respectively) (*6*, *17*, *41*). However, as demonstrated for another S = 2 Fe(IV)═O complex (*49*), a spectral splitting of about 5 mm/s can be observed if the hyperfine parameters are smaller than the isotropic Fermi-contact contribution of approximately −21 T, as is the case for $FeZn_4(moba)_4(btdd)_3$ (see also fig. S36).

S22). At these temperatures, it is possible that a greater quantity of Fe(IV)═O species is generated initially but that some of these sites react with the acetate ligand to generate a hydroxylated product and reform high-spin iron(II) sites. Analogous intramolecular α-C–H hydroxylation is known for α-ketoglutarate–dependent dioxygenases (*33*), and we discuss this possibility further below. Finally, spectra were collected at 5 K after heating the sample at 250 and 298 K without additional O_2 dosing. After warming at 250 K, the area of the Fe(IV)═O doublet was only 9.7(3)% and after warming at 298 K, the Fe(IV)═O doublet was absent, consistent with the decomposition observed in the DRIFTS data (fig. S20). A Mössbauer spectrum collected at 5 K after ex situ dosing of $FeZn_4(prv)_4(btdd)_3$ with O_2 at 163 K revealed a slightly higher Fe(IV)═O content of 32.2(6)% relative to that achieved under in situ conditions (section 2.9.2 of the SM and fig. S21), which may be due to the different conditions and the nature of the sample used (loose versus compact powder, respectively). The sample remained crystalline after warming to 298 K (fig. S25) and the porosity of the framework did not change significantly (1980 ± 23 m^2/g, fig. S26).

The Mössbauer isomer shift and quadrupole splitting values determined for the Fe(IV)═O species generated in $FeZn_4(prv)_4(btdd)_3$ are more consistent with an S = 2 than an S = 1 spin state, although these parameters alone do not enable an unambiguous assignment. To experimentally assign the spin state, we turned to applied magnetic field Mössbauer spectroscopy (*6*, *17*, *34*). We expected that the low concentration of the Fe(IV)═O species accessible upon dosing $FeZn_4(prv)_4(btdd)_3$ with O_2 would limit data resolution. One plausible explanation for the low detected concentration is decomposition of the Fe(IV)═O species through oxygenation of the newly formed acetate ligand (*33*). Such a side reaction would be precluded if pyruvate were replaced with an α-ketocarboxylate lacking α-C–H bonds. Accordingly, we synthesized $FeZn_4(moba)_4(btdd)_3$, which features a 3,3-dimethyl-2-oxobutyrate ligand with a *tert*-butyl group alpha to the carbonyl (see section 1.8 of the SM). This material is isostructural to $Fe_xZn_{5-x}(prv)_4(btdd)_3$ (fig. S27) and exhibits a comparably high BET surface area (fig. S28). In situ DRIFTS data collected for $FeZn_4(moba)_4(btdd)_3$ upon dosing with O_2 at 100 K support Fe(IV)═O formation through decarboxylation of 3,3-dimethyl-2-oxobutyrate [see fig. S29; ν(Fe = O) = 828 cm^{-1}, ν(Fe = ^{18}O) = 794 cm^{-1}], consistent with data discussed above for $FeZn_4(prv)_4(btdd)_3$.

The zero-field Mössbauer spectrum of $FeZn_4(moba)_4(btdd)_3$ collected at 5 K features a major doublet assigned to high-spin, five-coordinate iron(II) (fig. S31 and table S10). Following a sequence of in situ dosing with O_2 at 100 K and heating at 200 K, a new quadrupole doublet was apparent in the 5 K Mössbauer spectrum with δ = 0.292(1) mm/s and ΔE_Q = −0.603(1) mm/s [61.7(1)% area], assigned to the Fe(IV)═O species (fig. S31; the sign of the quadrupole splitting was determined from variable-field Mössbauer

data, see section 2.12 of the SM). This relative area is significantly larger than the maximum relative area of in situ O_2-dosed $FeZn_4(prv)_4(btdd)_3$ [21.1(1)%], supporting our hypothesis that intramolecular ligand oxygenation may be limiting the Fe(IV)═O content. Variable-field Mössbauer spectra were subsequently collected for O_2-dosed $FeZn_4(moba)_4(btdd)_3$ at 1.7 K under fields ranging from 0 to 7 T and at temperatures from 1.7 to 40 K under a field of 7 T (Fig. 3B and fig. S33; see section 2.12 of the SM). Spectra were also collected for $FeZn_4(moba)_4(btdd)_3$ at temperatures <5 K and fields ranging from 0 to 7 T (fig. S32) to obtain fixed parameters for modeling the residual iron(II) species for the O_2-dosed material (table S12; see section 2.12.2 of the SM).

Consistent with the zero-field Mössbauer spectrum collected at 5 K, the zero-field spectrum for O_2-dosed $FeZn_4(moba)_4(btdd)_3$ collected at 1.7 K could be fit with three subspectra, corresponding to an $S = 2$ iron(II) component, an iron(III) species, and an Fe(IV)═O component (Fig. 3B). The isomer shift of this Fe(IV)═O species is consistent with reported $S = 2$ iron(IV)–oxo species in the literature (fig. S40); however, both $S = 1$ and $S = 2$ models were considered in fitting the variable-field and variable-temperature data. Initial attempts to simultaneously fit the variable-temperature data collected under a 7 T field using this three subspectra model did not fully account for the total spectral intensity. We found that inclusion of a fourth subspectrum, assigned to an $S = 0$ species and likely arising from antiferromagnetically coupled Fe(IV)═O sites within the same cluster node, affords a good fit to the data (see section 2.12.3 of the SM). Although ICP-OES analysis predicts a distribution of one iron site per cluster on average, we cannot exclude a distribution wherein some clusters feature two iron centers per cluster, some feature a single iron center, and other clusters contain zero iron sites.

Simultaneous modeling of the variable-field and variable-temperature spectra was performed through diagonalization of the spin Hamiltonians for the four subspectra to obtain values of the zero-field splitting (D) and hyperfine coupling parameters (A_{xx}, A_{yy}, A_{zz}) for the uncoupled Fe(IV)═O species when assigned as either $S = 2$ or $S = 1$ (see section 2.12.3 of the SM for details and tables S13 to 15). Although the data could be fit with an $S = 2$ or $S = 1$ model (Fig. 3B and figs. S33 to S35), only the results for the $S = 2$ model are chemically reasonable based on a comparison with reported Fe(IV)═O species. The best model for the $S = 2$ Fe(IV)═O species yielded $D = 12.7(6)$ cm^{-1} and $a_{iso} = -16.4(4)$ T (table S13), parameters that are in excellent agreement with those reported for $S = 2$ Fe(IV)═O species ($D_{S=2} = 4$–14 cm^{-1}, $a_{iso(S=2)} = -23$ to -16 T) (*17*, *35*). By contrast, the best model for $S = 1$ Fe(IV)═O sites yielded values that are significantly different from those reported previously for $S = 1$ Fe(IV)═O species (table S14) (*35*–*37*). Furthermore, the signs and relative magnitudes of the spin-dipole contribution $\vec{A}_{SD}$ to the hyperfine coupling tensor are only consistent with an $S = 2$ spin ground state (see section 2.12.4 of the SM).

Additional experimental support for the $S = 2$ assignment for the Fe(IV)═O species was obtained from Fe Kβ x-ray emission spectroscopy (XES; section 2.13 of the SM). Iron Kβ XES involves the measurement of 3p to 1s emissions and because of the Fe 3p–3d exchange contributions to the final state, the relative intensities and energies of the Kβ mainline features—the Kβ′ and $K\beta_{1,3}$ peaks—are diagnostic of the local iron spin state (*38*–*40*). High-spin states typically give rise to more intense Kβ′ features and larger separations between the Kβ′ and $K\beta_{1,3}$ peaks than low-spin states (*39*). The XES spectra for $S = 2$ $FeZn_4(moba)_4(btdd)_3$ and a sample of the framework dosed ex situ with O_2 are given in fig. S39, along with a representative spectrum for a reported molecular compound featuring an $S = 1$ Fe(IV)═O (*40*). The spectra for pristine and O_2-dosed $FeZn_4(moba)_4(btdd)_3$ nearly overlay and feature an intense Kβ′ peak, consistent with the dominant presence of $S = 2$ iron sites in both materials. By contrast, there is no clear Kβ′ peak in the $S = 1$ Fe(IV)═O spectrum, and the $K\beta_{1,3}$ peak appears at a lower energy than in the spectrum for O_2-dosed $FeZn_4(moba)_4(btdd)_3$.

Finally, we used DFT to calculate Mössbauer isomer shifts for the model cluster $Fe(O)(\kappa^2\text{-}OPiv)Zn_4(prv)_3(bta)_6$ ($OPiv^-$, pivalate formed upon $moba^-$ decarboxylation; bta^-, benzotriazolate) featuring an $S = 2$ or $S = 1$ ground state. Geometry optimizations were performed at the BP86-D3BJ/def2-TZVP level of theory. For the $S = 2$ optimized geometry, $\delta_{calc} = 0.27$ mm/s is in excellent agreement with the experimentally determined isomer shift [$\delta = 0.292(1)$ mm/s], whereas the isomer shift calculated for $S = 1$ deviates significantly from the experimental value ($\delta_{calc} = 0.16$ mm/s) (table S11). Furthermore, CASSCF calculations in combination with *N*-electron valence perturbation theory to second order (NEVPT2) support the assignment of an $S = 2$ ground state, which is predicted to be 25 kcal/mol more stable than the lowest energy $S = 1$ configuration (see section 3 of the SM and fig. S41). Altogether, the Mössbauer, Fe Kβ XES, and computational data clearly support the assignment of an $S = 2$ ground state for the Fe(IV)═O sites formed upon oxidation of $FeZn_4(moba)_4(btdd)_3$.

Investigation of the local Fe(IV)═O coordination environment using nuclear resonance vibrational spectroscopy

Nuclear resonance vibrational spectroscopy (NRVS) was used to gain further insight into the local structure of the Fe(IV)═O species (see section 2.7 of the SM). This technique selectively yields the complete set of vibrational modes of Mössbauer-active nuclei and can therefore provide structural insights not accessible using other spectroscopic methods. Figure 4, A and B respectively, show the iron partial vibrational density of states (PVDOS) distributions obtained from data collected at ~100 K for desolvated 95% ^{57}Fe-enriched $FeZn_4(prv)_4(btdd)_3$ before and after ex situ O_2-dosing at 163 K. A new peak at 822 cm^{-1} for the O_2-dosed sample was assigned to an Fe(IV)═O vibration and is similar in magnitude to NRVS peaks reported for other nonheme Fe(IV)═O species in synthetic systems (*41*, *42*, *43*). In support of this assignment, when $^{18}O_2$ was employed for dosing, the vibration appeared instead at 788 cm^{-1} (Fig. 4B, inset; figs. S44 and S47). Consistent results were obtained from PVDOS distributions obtained for ^{57}Fe-enriched $FeZn_4(moba)_4(btdd)_3$ after dosing with O_2 or $^{18}O_2$ (fig. S50), which feature peaks at 820 and 789 cm^{-1}, respectively. The Fe(IV)═O peak was absent in the PVDOS distribution obtained for both frameworks after warming to 298 K (figs. S43 and S51).

Using the truncated cluster $FeZn_4(prv)_4(bta)_6$ as a model for $FeZn_4(prv)_4(btdd)_3$, we performed DFT calculations to simulate the NRVS iron PVDOS for the framework before and after O_2 dosing (Fig. 4, A and B, dark gray curves). The intense stretch at 330 cm^{-1} predicted for the model iron(II) framework corresponds to vibrations associated with bidentate pyruvate binding. Differences in the predicted and experimental intensities likely arise because the cluster model cannot fully describe the phonons of the framework lattice. For the O_2-dosed sample, stretches at 282 and 340 cm^{-1} are assigned as Fe–O vibrations resulting from κ^2-binding of the acetate ligand (Fig. 4C). By contrast, Fe–O vibrations associated with κ^1-binding of acetate are predicted to appear at higher wave numbers (>400 cm^{-1}) (figs. S45 and S46). The calculated Fe(IV)═O stretch is higher than the experimental stretching frequency (919 versus 822 cm^{-1}), likely because of a known systematic overestimation by DFT at these higher energies, which is less pronounced at lower energies (*44*). Finally, simulated NRVS iron PVDOS were also generated for pristine and O_2-dosed $FeZn_4(moba)_4(btdd)_3$ from DFT calculations on the truncated $S = 2$ cluster models $Fe(moba)Zn_4(prv)_3(bta)_6$ and $Fe(O)(\kappa^2\text{-}OPiv)Zn_4(prv)_3(bta)_6$, and the results are in good agreement with the experiment (figs. S48 and S49).

Reactivity studies

We evaluated the reactivity of $Fe_xZn_{5-x}(prv)_4(btdd)_3$ with hydrocarbon substrates in the presence of O_2. Desolvated $FeZn_4(prv)_4(btdd)_3$ was suspended in cyclohexane and exposed to one bar of O_2 at 21°C for 24 hours. Subsequently, CH_3CN-d_3 was added to extract the products, along with CH_2Br_2 as an internal standard. Analysis of the resulting supernatant using ^{1}H

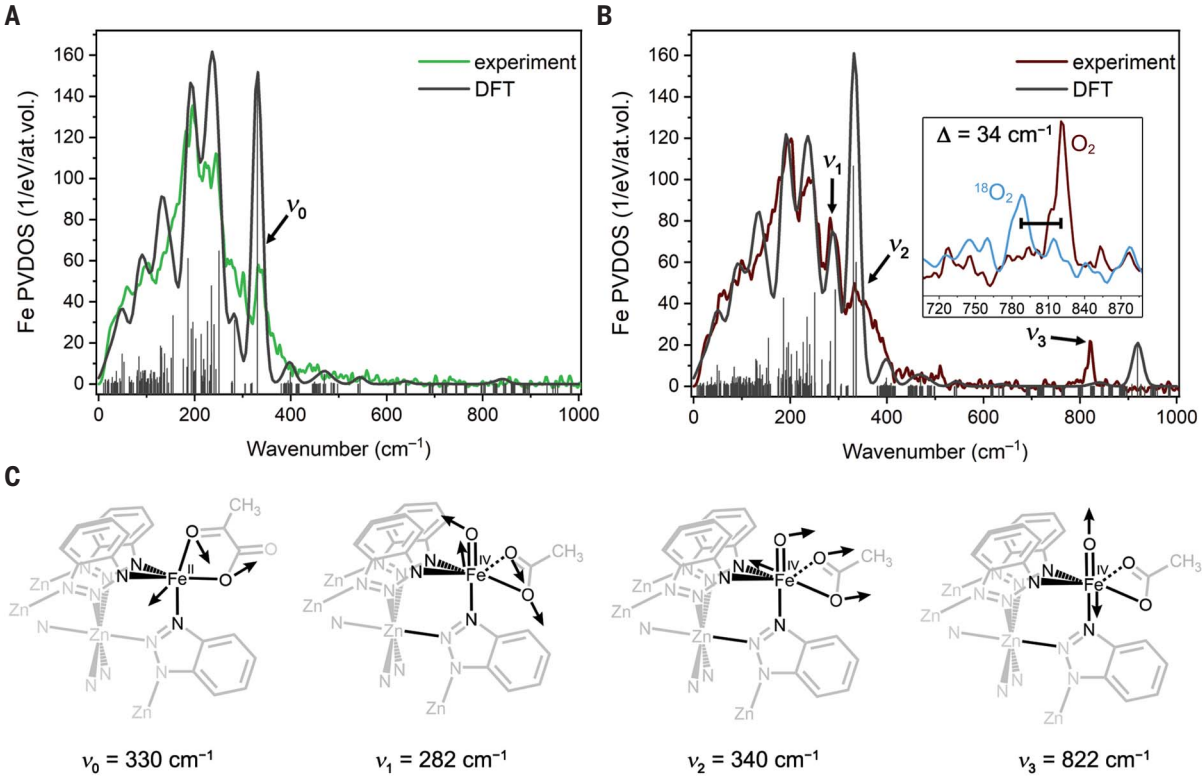

Fig. 4. Nuclear resonance vibrational spectroscopy (NRVS). (**A**) Iron partial vibrational density of states (PVDOS) distribution of ^{57}Fe-enriched, desolvated $FeZn_4(prv)_4(btdd)_3$ from NRVS data collected at ~100 K (green) and DFT computed Fe PVDOS for $FeZn_4(prv)_4(bta)_6$ (dark gray). (**B**) Iron PVDOS distribution of ^{57}Fe-enriched, desolvated $FeZn_4(prv)_4(btdd)_3$ obtained from NRVS data collected at ~100 K after dosing with 200 mbar of O_2 at 163 K (dark red) and DFT-computed PVDOS distribution for ~70% $FeZn_4(prv)_4(bta)_6$ and ~30% of $Fe(O)(\kappa^2\text{-}OAc)Zn_4(prv)_3(bta)_6$ (dark gray). The inset shows a shift of the Fe(IV)=O vibration to lower wave numbers (Δ = 34 cm^{-1}) when $^{18}O_2$ is used (light blue, see also fig. S46). Vertical lines indicate the individual vibrational transitions. (**C**) Assigned vibrational modes of $FeZn_4(prv)_4(btdd)_3$ and the O_2-dosed framework.

NMR spectroscopy and GC-MS revealed the formation of cyclohexanol (22% NMR yield with respect to the iron sites in the framework) with no detectable cyclohexanone (see section 1.9.1 of the SM and figs. S53 and S54). Mössbauer spectroscopy analysis of the framework isolated following this reaction revealed only iron(II) species (fig. S56). The same stoichiometric reaction was also carried out using $FeZn_4(moba)_4(btdd)_3$ in the presence of O_2 (1 bar, 21°C), and analysis of the resulting supernatant using ^{1}H NMR spectroscopy and GC-MS revealed the formation of only cyclohexanol (51% NMR yield) (see section 1.11.1 of the SM and figs. S59 and S60). A stoichiometric control reaction between cyclohexane and $FeZn_4Cl_4(btdd)_3$ in the presence of O_2 did not yield any hydrocarbon oxidation products (figs. S57 and S58).

In order to establish the direct role of the Fe(IV)=O species in C–H oxygenation, we sought to perform a stoichiometric reaction using a framework sample in which the Fe(IV)=O species were generated before the addition of substrate. A sample of $FeZn_4(prv)_4(btdd)_3$ was dosed with 200 mbar O_2 at 163 K and after 2 hours the sample headspace was evacuated and refilled with Ar; a mixture of cyclohexane and CD_2Cl_2 was then added. The suspension was then warmed to 195 K and held for 2 hours and then allowed to warm to 294 K. Under these conditions, no cyclohexane oxidation products were detected through ^{1}H NMR spectroscopy. When a similar reaction was performed using $FeZn_4(moba)_4(btdd)_3$ (see section 1.11.2 of the SM), ^{1}H NMR spectroscopy and GC-MS analysis of the resulting supernatant revealed the formation of cyclohexanone (figs. S61 and S62; 48% NMR yield). The ultimate formation of cyclohexanone in this case—in contrast to cyclohexanol formed in the reaction conducted at 21°C—is attributed to the lower reaction temperature and slower diffusion of cyclohexanol out of the framework pores, which is then further oxidized to cyclohexanone (see section 1.11 of the SM) (*45*).

When the cyclohexane oxidation reaction with $FeZn_4(prv)_4(btdd)_3$ was repeated with the addition of 11 equivalents of pyruvic acid, cyclohexanone and cyclohexanol were obtained in a 2:1 ratio (combined yield of 173%) (see section 1.9.2 of the SM and fig. S64). Powder x-ray diffraction analysis of the solid isolated from this reaction confirmed that the framework remains crystalline (fig. S65). Notably, this result suggests that $FeZn_4(prv)_4(btdd)_3$ can act as a catalyst in hydrocarbon oxidation reactions using the free α-keto acid as a co-substrate, presumably through a similar catalytic cycle as proposed for TauD (fig. S71) (*6*). We found that acetic acid byproduct is formed in this reaction in 288% yield with respect to the iron sites, which suggests 115% of pyruvic acid conversion to unidentified products. Such unproductive turnover at some of the iron sites is consistent with the relatively low yield in the stoichiometric reaction. A number of studies of synthetic and enzymatic systems have established that C–H bond activation by Fe(IV)=O species proceeds through H-atom abstraction, as evidenced by large primary kinetic isotope effects (KIEs) (*45*, *46*). Consistent with these results, we determined an intermolecular competition KIE value of 29.8 ± 1.0 from the reaction of $FeZn_4(prv)_4(btdd)_3$ with a mixture of cyclohexane and cyclohexane-d_{12} under an atmosphere of O_2 (see section 1.10 of the SM and figs. S66 and S67).

The reactivity of $Fe_{1.8}Zn_{3.2}(prv)_4(btdd)_3$ in the presence of O_2 was also evaluated using gaseous ethane as a substrate in a high-pressure batch reactor (section 1.12 of the SM). Using a high-pressure mixture of ethane and dioxygen, ethanol and acetaldehyde were obtained in a 3:1 ratio with a high combined yield of 82% (fig. S68). This yield is much higher than that obtained in

the stoichiometric cyclohexane oxidation, likely due to the high ethane concentration close to the iron sites under high pressure. Although there are enzymatic systems capable of oxidizing ethane to ethanol with O_2 (*47*), our result is the first synthetic example of ethane oxidation through an unambiguously characterized $S = 2$ Fe(IV)═O intermediate generated by O_2.

Outlook

We have developed the frameworks $Fe_xZn_{5-x}(prv)_4(btdd)_3$ and $FeZn_4(moba)_4(btdd)_3$ featuring iron(II) sites that activate O_2 at 100 K to form high-spin Fe(IV)═O species, reactivity that is reminiscent of O_2 activation in TauD. These frameworks are rare non-enzymatic systems capable of catalytic hydrocarbon oxygenation, including the oxidation of ethane to ethanol, through a reactive high-spin Fe(IV)═O intermediate generated from dioxygen. This work establishes a foundation for the development of iron-containing metal–organic frameworks as heterogeneous catalysts that closely mimic the reactivity of metalloenzymes.

REFERENCES AND NOTES

1. B. G. Hashiguchi *et al*., *Science* **343**, 1232–1237 (2014).
2. J. Shan, M. Li, L. F. Allard, S. Lee, M. Flytzani-Stephanopoulos, *Nature* **551**, 605–608 (2017).
3. V. L. Sushkevich, D. Palagin, M. Ranocchiari, J. A. van Bokhoven, *Science* **356**, 523–527 (2017).
4. E. G. Kovaleva, J. D. Lipscomb, *Nat. Chem. Biol.* **4**, 186–193 (2008).
5. C. Krebs, D. Galonić Fujimori, C. T. Walsh, J. M. Bollinger Jr., *Acc. Chem. Res.* **40**, 484–492 (2007).
6. J. C. Price, E. W. Barr, B. Tirupati, J. M. Bollinger Jr., C. Krebs, *Biochemistry* **42**, 7497–7508 (2003).
7. S. Sinnecker *et al*., *J. Am. Chem. Soc.* **129**, 6168–6179 (2007).
8. J. Hohenberger, K. Ray, K. Meyer, *Nat. Commun.* **3**, 720 (2012).
9. M. P. Mehn, K. Fujisawa, E. L. Hegg, L. Que Jr., *J. Am. Chem. Soc.* **125**, 7828–7842 (2003).
10. A. Thibon *et al*., *Angew. Chem. Int. Ed.* **47**, 7064–7067 (2008).
11. F. Li, K. M. Van Heuvelen, K. K. Meier, E. Münck, L. Que Jr., *J. Am. Chem. Soc.* **135**, 10198–10201 (2013).
12. D. Kass *et al*., *J. Am. Chem. Soc.* **142**, 5924–5928 (2020).
13. M. A. Dedushko, M. B. Greiner, A. N. Downing, M. Coggins, J. A. Kovacs, *J. Am. Chem. Soc.* **144**, 8515–8528 (2022).
14. J. P. Bigi *et al*., *J. Am. Chem. Soc.* **134**, 1536–1542 (2012).
15. M. Puri, L. Que Jr., *Acc. Chem. Res.* **48**, 2443–2452 (2015).
16. C. E. MacBeth *et al*., *Science* **289**, 938–941 (2000).
17. J. B. Gordon *et al*., *J. Am. Chem. Soc.* **143**, 21637–21647 (2021).
18. B. E. R. Snyder *et al*., *Nature* **536**, 317–321 (2016).
19. E. Tabor *et al*., *Sci. Adv.* **6**, eaaz9776 (2020).
20. B. Rungtaweevoranit *et al*., *ACS Appl. Mater. Interfaces* **15**, 26700–26709 (2023).
21. A. M. Wright *et al*., *Chem* **4**, 2894–2901 (2018).
22. C. E. Bien *et al*., *J. Am. Chem. Soc.* **140**, 12662–12666 (2018).
23. J. G. Vitillo, C. C. Lu, A. Bhan, L. Gagliardi, *Cell Rep. Phys. Sci.* **4**, 101422 (2023).
24. H.-C. Zhou, J. R. Long, O. M. Yaghi, *Chem. Rev.* **112**, 673–674 (2012).
25. H. Furukawa, K. E. Cordova, M. O'Keeffe, O. M. Yaghi, *Science* **341**, 1230444 (2013).
26. D. J. Xiao *et al*., *Nat. Chem.* **6**, 590–595 (2014).
27. A. Iliescu, J. J. Oppenheim, C. Sun, M. Dincă, *Chem. Rev.* **123**, 6197–6232 (2023).
28. A. Shaabani, R. Mohammadian, H. Farhid, M. K. Alavijeh, M. M. Amini, *Catal. Lett.* **149**, 1237–1249 (2019).
29. D. Denysenko, J. Jelic, K. Reuter, D. Volkmer, *Chemistry* **21**, 8188–8199 (2015).
30. D. Denysenko *et al*., *Chemistry* **17**, 1837–1848 (2011).
31. P. Gütlich, E. Bill, A. X. Trautwein, *Mössbauer Spectroscopy and Transition Metal Chemistry* (Springer, 2011).
32. D. A. Proshlyakov, T. F. Henshaw, G. R. Monterosso, M. J. Ryle, R. P. Hausinger, *J. Am. Chem. Soc.* **126**, 1022–1023 (2004).
33. M. G. Thompson *et al*., *Nat. Commun.* **11**, 2931 (2020).
34. V. Ksenofontov *et al*., *Hyperfine Interact.* **141**, 47–52 (2002).
35. A. R. McDonald, L. Que Jr., *Coord. Chem. Rev.* **257**, 414–428 (2013).
36. T. A. Jackson *et al*., *J. Am. Chem. Soc.* **130**, 12394–12407 (2008).
37. J. England *et al*., *Angew. Chem. Int. Ed.* **48**, 3622–3626 (2009).
38. N. Lee, T. Petrenko, U. Bergmann, F. Neese, S. DeBeer, *J. Am. Chem. Soc.* **132**, 9715–9727 (2010).
39. C. J. Pollock, M. U. Delgado-Jaime, M. Atanasov, F. Neese, S. DeBeer, *J. Am. Chem. Soc.* **136**, 9453–9463 (2014).
40. G. E. Cutsail 3rd *et al*., *Eur. J. Biochem.* **27**, 573–582 (2022).
41. V. F. Oswald *et al*., *J. Am. Chem. Soc.* **142**, 11804–11817 (2020).
42. C. B. Bell 3rd *et al*., *Angew. Chem. Int. Ed.* **47**, 9071–9074 (2008).
43. A. C. Weitz *et al*., *Angew. Chem. Int. Ed.* **57**, 16010–16014 (2018).
44. B. E. R. Snyder *et al*., *Proc. Natl. Acad. Sci. U.S.A.* **115**, 4565–4570 (2018).
45. A. N. Biswas *et al*., *J. Am. Chem. Soc.* **137**, 2428–2431 (2015).
46. J. C. Price, E. W. Barr, T. E. Glass, C. Krebs, J. M. Bollinger Jr., *J. Am. Chem. Soc.* **125**, 13008–13009 (2003).
47. P. Meinhold, M. W. Peters, M. M. Y. Chen, K. Takahashi, F. H. Arnold, *ChemBioChem* **6**, 1765–1768 (2005).
48. J. Börgel *et al.*, "Powder x-ray diffraction and iron Kβ x-ray emission spectroscopy data," Dryad (2023); https://doi.org/10.5061/dryad.wh70rxwtp.
49. K. Warm *et al*., *Angew. Chem. Int. Ed.* **60**, 6752–6756 (2021).

ACKNOWLEDGMENTS

We thank K. M. Carsch, T. D. Harris, A. Nguyen, J. Martell, R. Murphy, J. L. Peltier, M. Qi, B. E. R. Snyder, D. X. Ngo, X. Shen, and Y. Yang for helpful discussions. **Funding:** This research was supported by the US Department of Energy Office of Basic Energy Sciences under award DE-SC0019992. Single-crystal x-ray diffraction data were collected at beamlines 11.3.1 and 12.2.1 of the Advanced Light Source at Lawrence Berkeley National Laboratory, a user facility supported by the US Department of Energy, Office of Science, Office of Basic Energy Sciences, Chemical Sciences, Geosciences & Biosciences Division Heavy Element Chemistry Program under contract DE-AC02-05CH11231. Synchrotron powder x-ray diffraction data were collected on the 17-BM-B Beamline at the Advanced Photon Source, a US Department of Energy Office of Science User Facility operated by Argonne National Laboratory. NRVS data was collected at beamline 3-ID-B at the Advanced Photon Source. Use of the Advanced Photon Source at Argonne National Laboratory was supported by the US Department of Energy, Office of Science, Office of Basic Energy Sciences (contract DE-AC02-06CH11357). Work at the Molecular Foundry was supported by the Office of Science, Office of Basic Energy Sciences, US Department of Energy (contract DE-AC02-05CH11231). Instruments in the UC Berkeley College of Chemistry NMR facility are supported in part by NIH S10OD024998. EPR spectroscopic studies were funded by the National Institutes of Health (NIH 1R35GM126961 to R.D.B.). R.D.B. acknowledges support from the Miller Institute of Basic Research in Science, University of California, Berkeley. The computing cluster at the Molecular Graphics and Computation Facility at UC Berkeley is supported by NIH S10OD023532. The Fe Kβ XES measurements were carried out at the PINK beam line at the BESSY II electron storage ring operated by the Helmholtz-Zentrum Berlin für Materialien und Energie. D.J.S., S.P., E.B., D.A.P., S.D., and F.N. acknowledge the Max-Planck-Gesellschaft for funding. J.B. acknowledges the Deutsche Forschungsgemeinschaft for a Postdoctoral Research Fellowship. R.C.R. acknowledges the NASA Space Technology Graduate Research Opportunities fellowship. J.O. acknowledges the National Institute of General Medical Sciences for a Postdoctoral Research Fellowship under award F32GM143925. V.C. and M.V. acknowledge the Italian Ministry of University and Research for a Ph.D. fellowship awarded to M.V. and funding through PRIN2017 program (Project "Moscato" n° 2017KKP5ZR_004). **Author contributions:** K.H., J.B., and J.R.L. formulated the project. K.H. and J.B. synthesized the materials, collected and analyzed reactivity study data, and collected and analyzed the gas adsorption data. H.K., J.W.T., and A.B.T. collected and analyzed the single-crystal x-ray diffraction data. H.Z., H.M., X.L., and J.A.R. collected and analyzed the solid-state NMR spectra. D.J.S. collected the applied-field Mössbauer data. D.J.S., K.H., J.B., K.R.M., F.G., G.J.L., and F.N. analyzed the data. D.J.S. and E.B. collected and analyzed the MCD data. K.C. and R.D.B. collected and analyzed EPR data. C.D. and J.J.U. collected and analyzed the EDX data. Z.Z. collected and analyzed the thermogravimetric analysis data. J.G.P. collected and analyzed the magnetic susceptibility data. H.Z.H.J., K.H., and J.B. collected and analyzed the IR spectra. M.V.P., H.Z.H.J., K.H., J.B., J.O., M.V., and V.C. collected and analyzed the PXRD data. J.B., K.H., E.E.A., J.Z., M.Y.H., and B.L. collected and analyzed the NRVS data. K.H., J.B., R.C.R., F.G., and G.J.L. collected and analyzed the Mössbauer spectroscopy data. J.B., K.H., D.A.P., and F.N. performed the electronic structure calculations and analyzed the results. S.P. and S.D. collected and analyzed the Fe Kβ XES data. K.H., J.B., K.R.M., and J.R.L. wrote the manuscript, and all authors contributed to revising the manuscript. **Competing interests:** The University of California, Berkeley, has applied for a patent (International application no. PCT/US23/70362) on the synthesis of the iron containing metal–organic frameworks and their reactivity with hydrocarbon substrates in the presence of dioxygen, on which J.B., K.H., and J.R.L. are listed as coinventors. **Data and materials availability:** The supplementary materials contain complete experimental and spectral details for all new compounds reported herein. Single-crystal x-ray diffraction data have been made available free of charge from the Cambridge Crystallographic Data Centre under reference numbers CCDC 2166411 and 2166412. Powder x-ray diffraction and iron Kβ x-ray emission spectroscopy data are deposited in Dryad (*48*).

SUPPLEMENTARY MATERIALS

science.org/doi/10.1126/science.add7417
Materials and Methods
Supplementary Text
Figs. S1 to S71
Tables S1 to S17
References (*50–106*)
Data S1 and S2

Submitted 30 June 2022; resubmitted 15 June 2023
Accepted 24 September 2023
10.1126/science.add7417

Reactive high-spin iron(IV)-oxo sites through dioxygen activation in a metal–organic framework

Kaipeng Hou, Jonas Börgel, Henry Z. H. Jiang, Daniel J. SantaLucia, Hyunchul Kwon, Hao Zhuang, Khetpakorn Chakarawet, Rachel C. Rohde, Jordan W. Taylor, Chaochao Dun, Maria V. Paley, Ari B. Turkiewicz, Jesse G. Park, Haiyan Mao, Ziting Zhu, E. Ercan Alp, Jiyong Zhao, Michael Y. Hu, Barbara Lavina, Sergey Peredkov, Xudong Lv, Julia Oktawiec, Katie R. Meihaus, Dimitrios A. Pantazis, Marco Vandone, Valentina Colombo, Eckhard Bill, Jeffrey J. Urban, R. David Britt, Fernande Grandjean, Gary J. Long, Serena DeBeer, Frank Neese, Jeffrey A. Reimer, and Jeffrey R. Long

Science **382** (6670), . DOI: 10.1126/science.add7417

Editor's summary

Redox-active metalloproteins are often adept at binding to and controlling the reactivity of oxygen. Hou *et al*. showed that a metal-organic framework can similarly activate dioxygen and perform hydroxylation of aliphatic substrates. The authors used a range of spectroscopic techniques to demonstrate that the mechanism proceeds through a high-spin iron(IV) oxo species, similar to what is seen in some dioxygenase enzymes. This system can perform catalytic oxygenation of cyclohexane and should inspire future catalyst development for dioxygen activation and hydrocarbon oxidation. —Michael A. Funk